

High amplitude, high frequency harmonic modulation of rotating
Rayleigh-Bénard convection can more than quadruple heat
transfer

Liesbeth Klein Kranenburg

May 27, 2020

Onderzoek van Wiskunde, 20 EC
Educatie en Communicatie in de Bètawetenschappen
Faculty of Behavioural, Management and Social Sciences
University of Twente

Committee:

Prof. Dr. Ir. Bernard Geurts
Multiscale Modeling and Simulation

Assistant Prof. Dr. Richard Stevens
Physics of Fluids

Abstract

In harmonically modulated rotating Rayleigh-Bénard convection (MRRB) a time-dependent angular velocity $\Omega(t) = \Omega_0 + \Delta\Omega \sin(\omega t)$ is added to a RB system. Earlier research by (Niemela et al., 2010), (Geurts and Kunnen, 2014) and (Beunen and Kunnen, 2019) suggests possible great enhancement of heat transfer in these systems. We report on Direct Numerical Simulations (DNS) in a standardized system with water as a working fluid ($\text{Ra} = 10^8, \text{Pr} = 6.4$) in a cylindrical cell with height $H = 1$ and diameter $D = 1$. Modulated rotation introduces an Euler force into the governing equations which depends on the frequency and amplitude of the modulation only, as the constant rotation rate is set to zero. Two parameter sweeps for amplitudes were carried out at two different frequencies, complementing earlier simulations performed by Beunen (Beunen and Kunnen, 2019) as well as providing an entirely new data set. An impressive increase in Nusselt number of about 335% compared to the non-rotating case was achieved for a modulation with non-dimensional Rossby numbers for amplitude $\text{Ro}^* = 0.01$ and frequency $\text{Ro}_\omega = 0.1$. No optimal value of these Rossby numbers was found, but rather an asymptotic region where results suggest a scaling law $\text{Nu} \sim (\text{Ro}^*)^{-0.45}$ for amplitudes $\text{Ro}^* < 0.2$ and seemingly independent on frequency. Underlying flow structures include very efficient mixing at the top and bottom plates and a large temperature gradient at half height near the sidewalls. The flow is dominated by fluctuations in the θ -direction due to the extra Euler force. The underlying flow structure in the $r - z$ plane shows a stable double convection roll which might explain the efficiency of heat transfer in these cases. Further research into the influence of the frequency or fluid properties such as the Rayleigh and Prandtl numbers will deepen the understanding of this behaviour, possibly resulting in interesting industrial applications of this extremely efficient heat transfer.

Contents

1	Introduction	4
2	Mathematical model and numerical setup	5
3	Qualitative changes under high amplitude modulation	11
4	Increased Nusselt number for high amplitude, high frequency modulation	14
5	Concluding remarks	15
6	Appendix	17

1 Introduction

Rayleigh Bénard (RB) convection is a type of natural convection where fluid is heated from below and cooled from above. A turbulent flow pattern will emerge because of buoyancy effects on the one hand, and viscous and diffusive effects on the other hand. The expected flow pattern is a large scale circulation (LSC) which may switch directions due to the turbulent nature of the flow (Stevens et al., 2012). RB convection occurs in several geophysical and astrophysical systems. For example, in the Earth's outer core (Glatzmaier et al., 1999), the atmosphere (Sidorenkov, 2009), or in the outer layer of the sun (Cattaneo et al., 2003). Here we consider RB convection in a cylindrical domain with diameter $D = 1$ and height $H = 1$. Furthermore we choose dimensionless temperatures to be $T_b = 1$ on the bottom plate and $T_t = 0$ on the top plate, so that we have a temperature difference $\Delta T = 1$. In Figure 1 a sketch can be found.

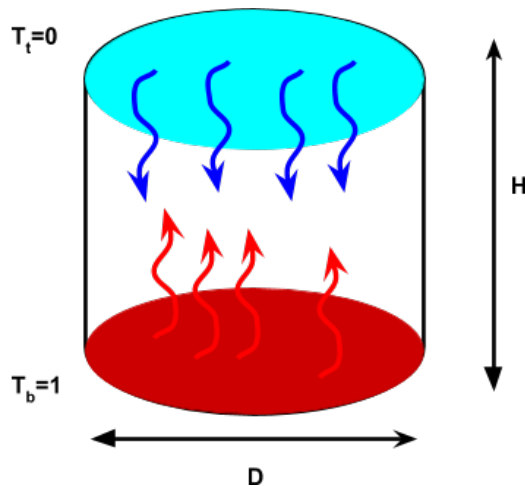


Figure 1: Sketch of non-rotating Rayleigh-Bénard convection in a cylindrical domain.

In general, RB studies look into the heat transfer between the bottom and top plate and its relation to various input parameters. The heat transfer is often quantified by the dimensionless Nusselt number, whereas fluid properties are captured in the Rayleigh and Prandtl number. Extensive research has been done on finding the optimal Nusselt number for a certain combination of Prandtl and Rayleigh number. This has been achieved for example by adding a constant rotation rate Ω in the θ -direction of the cylinder in so called rotating Rayleigh-Bénard (RRB) convection, achieving an increase of about 15% in the Nusselt number for moderate rotation rates (Stevens et al., 2013). It can also be done by optimizing the ratio between the diameter and the length, resulting in an increase in heat transfer of about 12% (at $Ra = 10^8$) (Chong et al., 2015).

This thesis concerns the relatively new field of modulated rotating Rayleigh-Bénard (MRRB) convection, where the rotation rate is not constant, but can instead be defined as: $\Omega = \Omega(t)$. In this research we will look into harmonic MRRB convection, further defining $\Omega(t)$ as:

$$\Omega(t) = \Omega_0 + \Delta\Omega \sin(\omega t), \quad (1)$$

where we have the time dependent rotation rate $\Omega(t)$, the constant rotation rate Ω_0 , the modulated rotation rate $\Delta\Omega$ and the angular velocity of the modulated rotation rate ω . This type of ‘shaking’ RB flow might not be directly relevant to large scale systems in nature, but could develop interesting industrial applications due to the extreme enhancement of heat transfer found in these systems. The first results were found by (Niemela et al., 2010) who did an unique experiment with cryogenic helium gas as a working fluid for high Rayleigh numbers and a high modulation angular velocity. In their experiments they found impressive enhancements in the heat transfer for the MRRB situation. In 2014 Geurts & Kunnen further looked into this, but this time with Direct Numerical Simulations (DNS) and using the properties of water for their model, as well as working with a lower Rayleigh number of 10^9 (Geurts and Kunnen, 2014). They found interesting results, but later found out that the implementation of the Euler force had an incorrect specification of the modulation amplitude. While the reported large increase in Nu can be maintained, the actual quantitative values needed correction. In 2019 Bob Beunen, a student at the TU/e, continued their work with a corrected version of the same code and a slightly lower Rayleigh number $Ra = 10^8$ and found enhanced heat transport for high amplitude and high frequency MRRB convection and an indication of even higher Nusselt numbers for even higher amplitudes (Beunen and Kunnen, 2019). This thesis builds on his results and complements them with extra simulations at the same frequency for higher amplitudes and provides an additional simulation set at an even higher

frequency. Our results confirm his hypothesis and we achieve an incredible quadrupled Nusselt number compared to the non-rotating case, as well as consistent flow structures that indicate an asymptotic behaviour such that Nusselt could increase even more for even lower modulation amplitudes.

The report is organized as follows: Section 2 provides the relevant mathematical model and numerical setup, as well as an analysis of the time averaging and resolution accuracy. Then, Section 3 contains various flow representations that will give some insight into the underlying flow structure. Subsequently, Section 4 shows and discusses the main results for the Nusselt numbers and a possible scaling law. Lastly, in Section 5 some ideas regarding future research will be discussed.

2 Mathematical model and numerical setup

Boussinesq Approximation

For incompressible, Newtonian flow, the Navier-Stokes equations reduce to:

$$\frac{\partial \vec{u}}{\partial t} + (\vec{u} \cdot \vec{\nabla}) \vec{u} = -\frac{1}{\rho} \vec{\nabla} \vec{p} + \nu \vec{\nabla}^2 \vec{u} + \frac{1}{\rho} \vec{F}, \quad (2)$$

where \vec{u} denotes the velocity, t denotes the time, ρ is the density, \vec{p} denotes the pressure, ν is the kinematic viscosity and F are the forces that are present in the system: buoyancy forces and rotational forces. Furthermore, since we approximate our system as having incompressible flow, we get a simplified continuity equation of:

$$\vec{\nabla} \cdot \vec{u} = 0 \quad (3)$$

For the modelling of our MRRB convection we can use the Boussinesq approximation. This approximation ignores all differences in fluid properties, except for those in density and only considers fluctuations in density when they are multiplied by g , the gravitational acceleration. Within this approximation we model the changes in density as being linear with temperature:

$$\rho = \rho_0 - \alpha \rho_0 \Delta T \quad (4)$$

where ρ_0 is some reference density, α is the thermal expansion coefficient and ΔT is the temperature difference between the upper and lower plate of the system.

Besides buoyancy forces we also have rotational forces due to the modulated rotation $\Omega(t)$. In order to derive the equations governing this rotation, we need to look at a stationary reference frame I and a rotational reference frame R . The velocities of these respective frames are related as follows:

$$\left(\frac{d\vec{r}}{dt} \right)_I = \left(\frac{d\vec{r}}{dt} \right)_R + \vec{\Omega}(t) \times \vec{r} \quad (5)$$

For the Navier-Stokes equation we need the force, so we need to calculate the acceleration by applying the same operator twice:

$$\left(\frac{d^2 \vec{r}}{dt^2} \right)_I = \left(\left(\frac{d}{dt} \right)_R + \vec{\Omega}(t) \right)^2 \times \vec{r} \quad (6)$$

$$= \left(\frac{d^2 \vec{r}}{dt^2} \right)_R + \underbrace{2\vec{\Omega}(t) \times \left(\frac{d\vec{r}}{dt} \right)_R}_{\text{Coriolis force}} + \underbrace{\vec{\Omega}(t) \times \vec{\Omega}(t) \times \vec{r}}_{\text{centrifugal force}} + \underbrace{\frac{d\vec{\Omega}(t)}{dt} \times \vec{r}}_{\text{Euler force}} \quad (7)$$

The buoyancy forces follow from Equation 4, and the rotational forces follow from Equation 7, resulting in the modified N-S equation:

$$\frac{\partial \vec{u}}{\partial t} + (\vec{u} \cdot \vec{\nabla}) \vec{u} = -\frac{1}{\rho_0} \vec{\nabla} \vec{p} + \nu \vec{\nabla}^2 \vec{u} + g\alpha T \vec{z} - 2\vec{\Omega}(t) \vec{z} \times \vec{u} - r \frac{d\vec{\Omega}(t)}{dt} \vec{\theta}, \quad (8)$$

where the centrifugal forces are contained in the pressure term.

The third governing equation for Rayleigh-Bénard convection is the convection-diffusion equation:

$$\frac{\partial T}{\partial t} + (\vec{u} \cdot \vec{\nabla}) T = \kappa \nabla^2 T \quad (9)$$

Non-dimensional model

To simplify computations and generalize the flow behaviour, we will non-dimensionalize the three main equations 3, 8 and 9. To do this we need to introduce some dimensionless variables:

$$l = Hl^*, \quad (10)$$

$$t = \frac{H}{U}t^*, \quad (11)$$

$$p = \rho_0 U^2 p^*, \quad (12)$$

$$T = \Delta T T^*, \quad (13)$$

$$u = U u^*, \quad (14)$$

$$\nabla = \frac{1}{H} \nabla^*, \quad (15)$$

where l denotes all length scales, $H = 1$ is the height of the cylinder and $U = \sqrt{g\alpha\Delta TH}$ is the typical velocity. Rewriting Equation 8 with these dimensionless variables gives the following equation:

$$\frac{\partial \vec{u}^*}{\partial t^*} + (\vec{u}^* \cdot \vec{\nabla}^*) \vec{u}^* = \vec{\nabla}^* p^* + \sqrt{\frac{\text{Pr}}{\text{Ra}}} (\vec{\nabla}^*)^2 \vec{u}^* + T^* \hat{z} - \frac{1}{\text{Ro}} \hat{z}^* \times \vec{u}^* - \frac{r^*}{4\text{Ro}_\omega \text{Ro}^*} \cos\left(\frac{t^*}{2\text{Ro}_\omega}\right) \hat{\theta}, \quad (16)$$

where we use the following dimensionless numbers:

$$\text{Ra} = \frac{g\alpha\Delta TH^3}{\nu\kappa}, \quad (17)$$

$$\text{Pr} = \frac{\nu}{\kappa}, \quad (18)$$

$$\text{Ro} = \frac{U}{2H\Omega}, \quad (19)$$

$$\text{Ro}_0 = \frac{U}{2H\Omega_0}, \quad (20)$$

$$\text{Ro}^* = \frac{U}{2H\Delta\Omega}, \quad (21)$$

$$\text{Ro}_\omega = \frac{U}{2H\omega}, \quad (22)$$

where the Rayleigh number (Ra) gives a general indication of the flow behaviour and gives the ratio between the time scales of diffusion and convection and the Prandtl number (Pr) is defined as the ratio between momentum diffusivity and thermal diffusivity. The various Rossby numbers (Ro) represent how a flow is affected by rotational forces and have the non-dimensional relation:

$$\frac{1}{\text{Ro}}(t^*) = \frac{1}{\text{Ro}_0} + \frac{1}{\text{Ro}^*} \sin\left(\frac{t^*}{2\text{Ro}_\omega}\right), \quad (23)$$

which can be derived from Equation 1.

The continuity equation (Equation 3) can also be non-dimensionalized:

$$\frac{U}{H} \vec{\nabla}^* \cdot \vec{u}^* = 0, \quad (24)$$

$$\vec{\nabla}^* \cdot \vec{u}^* = 0 \quad (25)$$

Lastly the convection-diffusion equation has the non-dimensionalized form:

$$\frac{\partial T^*}{\partial t^*} + (\vec{u}^* \cdot \vec{\nabla}^*) T^* = \frac{1}{\sqrt{\text{PrRa}}} \nabla^{*2} T^*. \quad (26)$$

Numerical model

Since our simulation is in a cylindrical domain, it is convenient to use cylindrical coordinates. The Navier-Stokes equations under the Boussinesq approximation can be rewritten to cylindrical fluxes using:

$$q_r = r \cdot u_r, \quad (27)$$

$$q_\theta = u_\theta, \quad (28)$$

$$q_z = u_z, \quad (29)$$

where q_r, q_θ, q_z represent the fluxes in the r, θ, z -directions respectively. For the DNS we use a finite-difference flow solver as first proposed by (Verzicco and Orlandi, 1996) with modifications for MRRB by (Geurts and Kunnen, 2014). This simulation employs a third order Runge-Kutta scheme to integrate the discretized non-dimensional equations by making use of cylindrical fluxes to model the flow field. A staggered grid is used, which means that vector quantities are evaluated at the edges of the grid, while scalar quantities such as the temperature or the pressure are evaluated at the center of a grid cell, see Figure 2. Since $q_r = r \cdot u_r$, this flux will automatically be zero at the center axis $r = 0$ preventing any problems. More details can be found in (Verzicco and Orlandi, 1996).

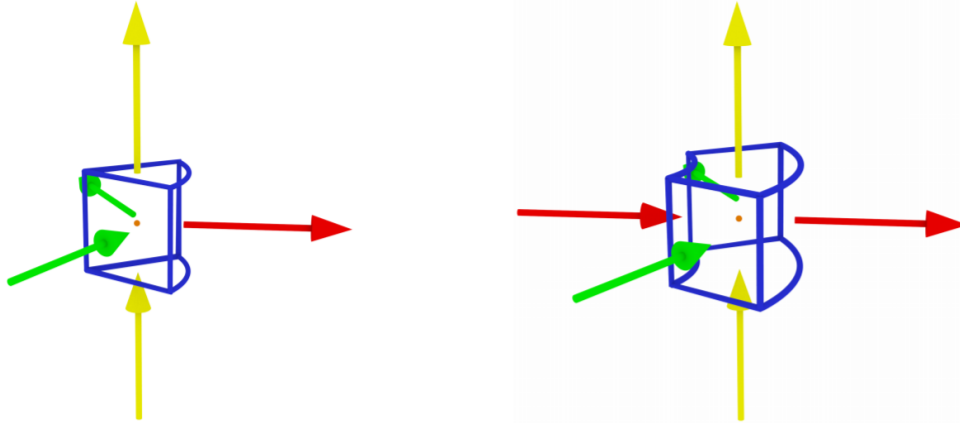


Figure 2: Sketch of a grid cell in the center of the cylinder (left) and away from the center (right). Blue lines: outlines of the cell; Yellow arrows: q_z ; Green arrows: q_θ ; Red arrows: q_r ; Orange dot: evaluation point for scalar quantities. Figure taken from (Beunen and Kunnen, 2019).

Nusselt number

Within this non-dimensional model, we also use a non-dimensional number to quantify the heat transfer, the Nusselt number:

$$Nu = \frac{\text{Convective heat transfer}}{\text{Conductive heat transfer}} = \frac{\langle Q \rangle H}{k \Delta T}, \quad (30)$$

where $\langle Q \rangle$ is the average heat flux density, k is the thermal diffusivity, and $H, \Delta T$ are defined as before. For our situation the Nusselt number calculation can be simplified in two ways. Firstly as a volume and time average over the entire domain:

$$\overline{Nu} = 1 + \sqrt{\text{PrRa}} \langle q_z T \rangle_{V,t}, \quad (31)$$

where \overline{Nu} denotes the volume averaged Nusselt number and $\langle q_z T \rangle_{V,t}$ denotes the time and volume average over the vertical flux times the temperature at some interval. Secondly, Nusselt can be evaluated at the plates by computing the local flux:

$$Nu_{0,1} = - \left\langle \frac{\partial T}{\partial z} \right\rangle_{A,t} \Big|_{z=0,1}, \quad (32)$$

where Nu_0 and Nu_1 denote the Nusselt numbers evaluated at the bottom and top plates respectively (Kunnen, 2008). Within the code, output data from both these methods is available. In the file ‘nusse.out’ the volume averaged data is collected (Equation 31), whereas the file ‘boute.out’ collects data for the Nusselt evaluations at both plates (Equation 32). The three data sets will be used to compare amongst each other as an indication of statistical stability and to obtain a more reliable average value of the Nusselt number. More details about time averaging can be found in the dedicated subsection below.

Simulation	Ro_ω	Ro^*
S0	∞	∞
S1	0.2	0.125
S2		0.1
S3		0.05
S4		0.02
S5		0.4
S6	0.1	0.2
S7		0.1
S8		0.08
S9		0.05
S10		0.02
S11		0.01

Table 1: Overview of conducted simulations. All simulations were performed for $Ro_0 = 10^{10}$ ($\Omega_0 \approx 0$), $Ra = 10^8$, $Pr = 6.4$ with resolution $n_\theta = 257, n_r = 129, n_z = 257$.

Conducted simulations

As mentioned before we base ourselves on the simulations done by Bob Beunen. We supplement these with three extra simulations for the same frequency $Ro_\omega = 0.2$. In addition we provide seven simulations at frequency $Ro_\omega = 0.1$. As a baseline we have simulated the non-rotating case. In table 1 an overview of conducted simulations can be found. All MRRB simulations (S1-S11) were restarted from the non-rotational simulation (S0) as this results in a faster converging rate (Beunen and Kunnen, 2019).

Time series of the Nusselt number

In Figure 3 one can see a typical example of a Nusselt time series. The simulation reaches a statistically stationary state after about 80 non-dimensional time units (Beunen and Kunnen, 2019). To be on the safe side a cut-off time after 300 non-dimensional time units was therefore chosen. Using this cut-off time, an average value Nusselt was calculated by taking the time average over the remaining 200 time steps. Figure 4 shows the time convergence of the Nusselt number for the same example as used in Figure 3. The Nusselt value converges to a 95% confidence interval of 78.11 ± 0.55 , or a time averaging error $< 1\%$ with this time averaging method. Decreasing this time averaging error would require a significant increase in simulation time, while the current method is sufficiently accurate for all purposes of this study.

In addition to averaging over time, the determination of the Nusselt number was further improved by averaging over the three data sets that use different methods of evaluating the Nusselt number. In all our simulations these three different Nusselt numbers, $\overline{Nu}, Nu_{0,1}$, were within a 1% margin of each other, suggesting that our simulation results are accurate.

Resolution requirements

For simulation S9 a resolution analysis was performed. In Figure 5 the values of Nusselt can be seen for different numbers of grid points. In our main simulations a grid of $257 \times 129 \times 257$ was used, which corresponds to a total amount of grid points $N \approx 8.5 \times 10^6$, as illustrated in Figure 5 by the vertical dashed line. The Nusselt values for this resolution do not seem to match the horizontal black lines, this is because the main simulations were restarted from 200 non-dimensional time units of non-rotating RB convection and were time averaged over 300 non-dimensional time units instead of 100. Therefore more accurate values, as represented by the horizontal lines, have been achieved. The fact that these lines correspond to the Nusselt number for the finest grid confirms that the resolution that was used, in combination with the time averaging technique as discussed before, provides an accurate determination of the Nusselt number under these input parameters.

As a first indication of convergence it's good to look at the three differently calculated values of the Nusselt number to see if they converge. However, this does not automatically imply that the resolution is adequate. Besides looking at the convergence of the Nusselt number it is also important to look at how the underlying flow structures are captured. In general it holds that if underlying flow structures are well-captured, then the Nusselt number is also well-captured, but not necessarily the other way around (Kooij et al., 2018). A way to check this is to plot the temperature gradient along a line and look at the amount of grid points that capture a temperature change. In this case two vertical lines were chosen in the bulk of the flow and close to the sidewall respectively. Figure 11 in the appendix shows the temperature gradient across these lines for simulations S9 and S10. It appears that even though for both simulations

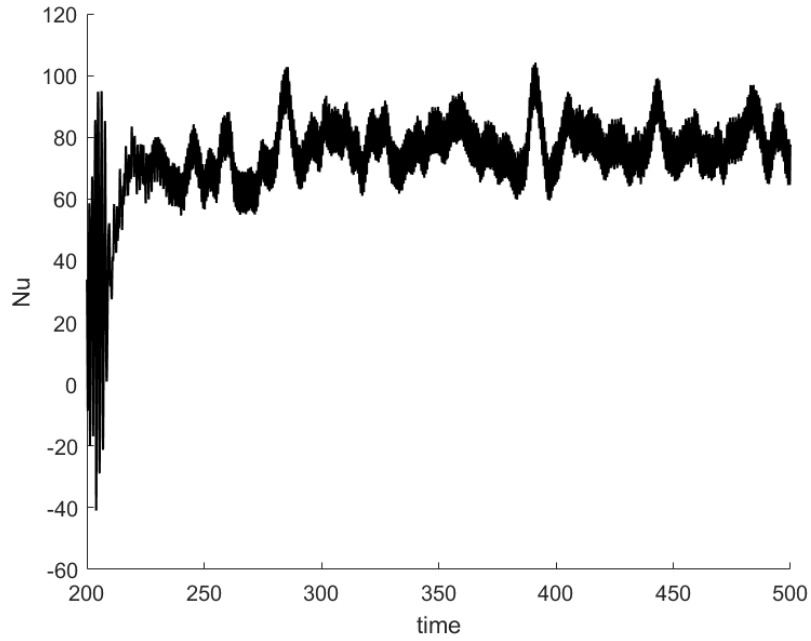


Figure 3: Typical time series of the Nusselt number. This example is taken from the volume averaged evaluation (Equation 31) of simulation S9 ($Ro_\omega = 0.1$, $Ro^* = 0.05$).

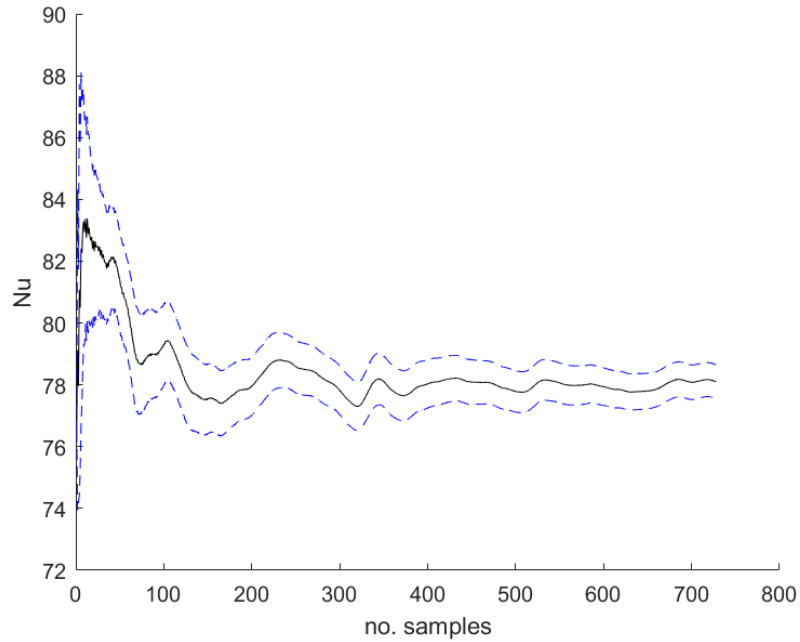


Figure 4: Nusselt number from the volume averaged evaluation (Equation 31) of simulation S9 ($Ro_\omega = 0.1$, $Ro^* = 0.05$) for different amounts of time averaging samples. Black solid line: average value of Nusselt; blue dashed line: 95% confidence interval.

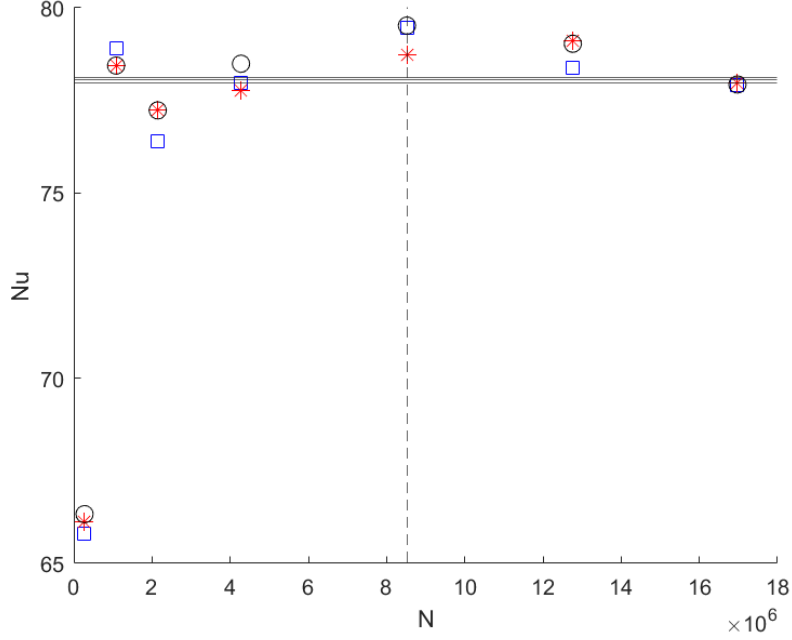


Figure 5: Time averaged values of \overline{Nu} (blue squares), Nu_1 (red asterisks) and Nu_0 (black circles) on a semilog scale. Here N is the total amount of grid cells $n_\theta \times n_r \times n_z$. The vertical dashed line represents the resolution used in all simulations. The horizontal black lines represent the three values from simulation S9 ($Ro_\omega = 0.1$, $Ro^* = 0.05$) with a restart from the non-rotational simulation and a longer time-averaging period.

S9 and S10 the three different time averages of Nusselt coincide within a 1% margin, simulation S10 does not seem to have an adequate amount of grid points to adequately capture temperature gradients within the underlying flow structure.

It is therefore that simulations S4, S10 and S11 (with $Ro^* \leq 0.02$) will be considered merely an indication of an achievable Nusselt number, while the other simulations can be expected to be accurate depictions of fluid behaviour under these conditions. It is possible that due to this lower resolution the value of Nusselt has been overshoot slightly (see Figure 5), however the consistency in Nusselt number over the three different evaluations strongly suggests that the qualitative increase of the Nusselt number is still valid. In the scope of this master thesis it was not possible to redo these simulations at a higher resolution. Simulation times already exceeded four weeks for these high amplitude cases, so in order to increase the resolution it would be necessary to decrease simulation times, for example by performing them on parallel cores.

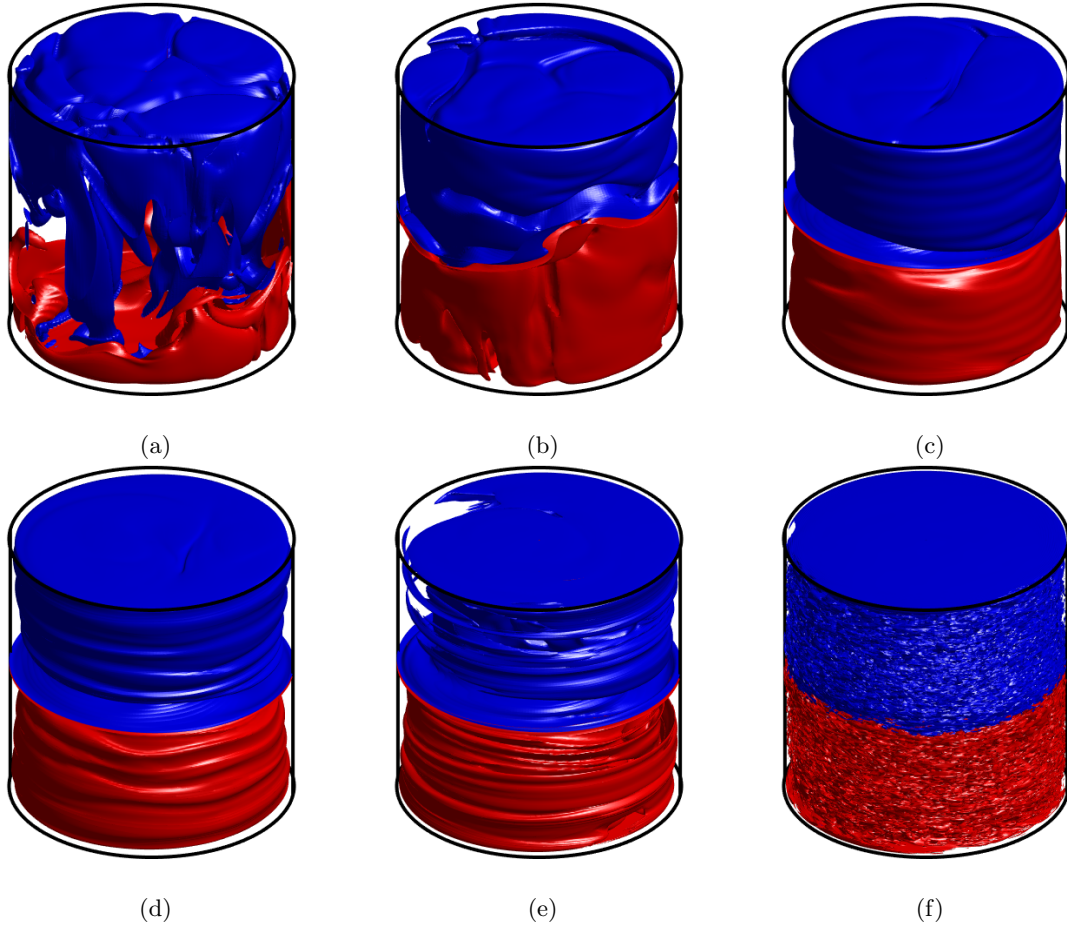


Figure 6: Isosurfaces for $T^*=0.45$ (blue) and $T^*=0.55$ (red). (a) Non-rotational simulation at $time = 200$; (b-f) $Ro_\omega = 0.1$ at $time = 500$ for $Ro^*=0.4$ (b), $Ro^*=0.2$ (c), $Ro^*=0.1$ (d), $Ro^*=0.05$ (e), $Ro^*=0.02$ (f)

3 Qualitative changes under high amplitude modulation

Two important qualitative changes can be seen in the flow structure under MRRB convection: high mixing at the plates, and a large temperature gradient at half height near the sidewall. This can be illustrated for example by looking at isosurface plots of flow snapshots, see Figure 6. These figures indicate that the flow structure transitions from vertical plumes into two more or less homogeneous halves that meet in the middle of the cylinder. At the upper plate it can further be seen that the temperature field close to the plate is completely smoothed out for high amplitude modulation in contrast to the cell structure that can be seen for the non-rotational case. As mentioned in section 2 the simulation for $Ro^*=0.02$ suffers from a low amount of grid points compared to the size of the flow structures. This can be seen in Figure 6f as the isosurface looks grainy, indicating rough gradients of the temperature field. For the higher amplitude, and therefore larger Euler force it seems that either small scale structures are more present in the flow or the rate of change of the temperature increases. Both effects might cause this under-captured isosurface plot.

Contour plots at various heights (Figure 7) show clearly that mixing close to the plates is more efficient for higher amplitude modulation. In Figure 7m we can see the two more or less homogeneous halves meet in the middle, resulting in sharp temperature gradients. Figure 15 in the appendix further highlights this sharp temperature gradient at half height along vertical rings near the sidewall.

Furthermore the in-code statistical tools were used to obtain average and RMS values for temperature, pressure and velocity (Verzicco and Orlandi, 1996). These have been averaged both over time and over the angular direction. The most interesting effects can be seen for the temperature fluctuations (RMS values) in Figure 12 and for the mean vertical velocity in Figure 13, both in the appendix. The temperature fluctuations confirm that fluctuations close to the top and bottom plates are damped, while fluctuations at half height increase for higher modulation amplitudes. In Figure 13 we can see that we get a horizontal division line at half height and a vertical division line around $r = 0.35$ which divides the cylinder in four approximately equal volume sections. In addition to this division it can also be seen that the mean (absolute) axial velocity gets larger for higher amplitude modulation by a factor of about 2 between

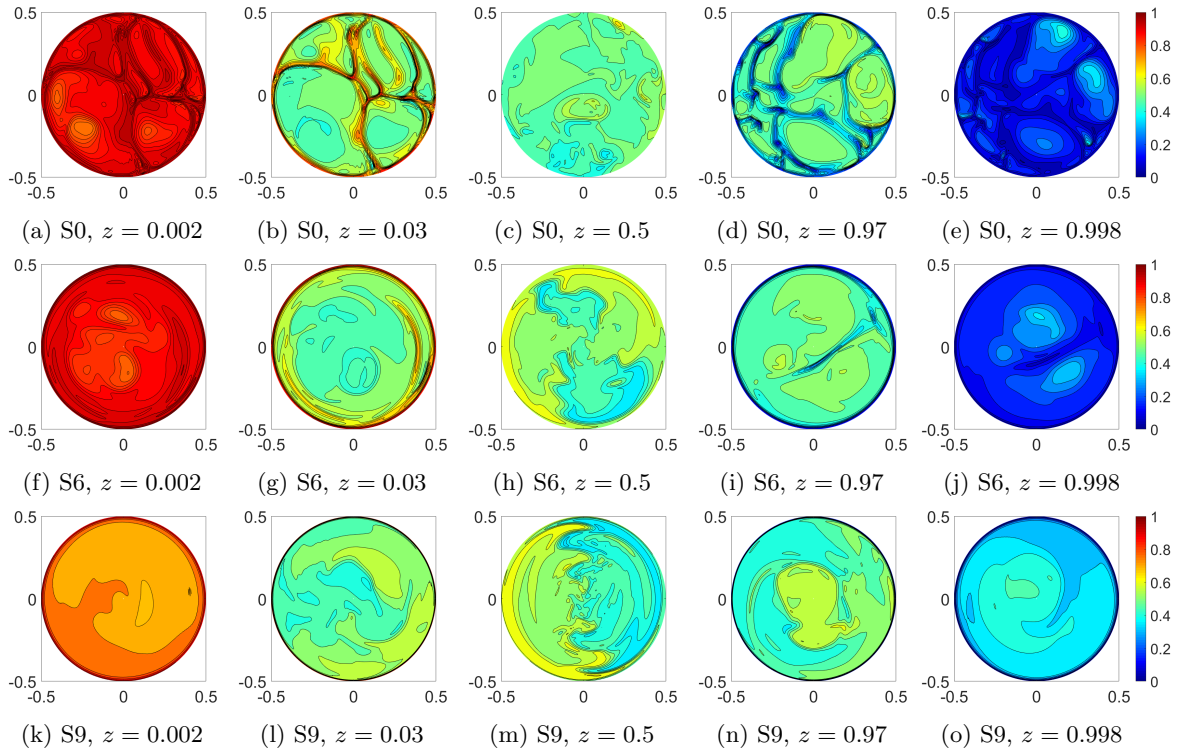


Figure 7: Horizontal cross-sections of three flow snapshot for simulations S0 (non-rotational) at $time = 200$, S6 ($Ro^*=0.2$) at $time = 500$ and S9 ($Ro^*=0.05$) at $time = 500$ at various heights. Same colours represent the same temperature, dark blue: $T = 0$ and dark red: $T = 1$.

figures 13c and 13d. This increase in axial velocity might be caused by a more efficient heat transport. For simulation S9 ($Ro_\omega = 0.1, Ro^* = 0.05$) additional flow statistics can be found in figure 14 in the appendix. From the mean radial velocity, figure 14a and the mean axial velocity as in figure 13d, we expect that there is a sort of double convection roll structure in the $r-z$ plane, underneath the extremely dominant fluctuations in the angular direction (Figure 14b). This is illustrated in Figure 8 where the mean axial and radial velocities are combined in a vector plot. The flow structure under MRRB convection seems to consist of a counterclockwise convection roll at the bottom plate and a clockwise convection roll at the top plate, that meet at half height. It can also be seen in Figure 14 that the axial and radial fluctuations are very small compared to the angular fluctuations. This $r-z$ flow structure is thus relatively stable. Whereas the vector plots in Figure 8 only show relative motion, in Figure 13 we can see that the (absolute) mean velocity in the axial direction increases for higher amplitude modulation.

For RRB convection it is known that for higher rotation rates fluid motion in the axial direction is suppressed, which is called the Taylor-Proudman effect (Wu et al., 2006). This would generally be balanced by the effect of Ekman pumping, where thermal plumes become vortices due to the rotational forces and efficiently suck hot (cold) fluid from the bottom (top) plate to transport it vertically (Stevens et al., 2013). In geometrically confined RB convection heat transport is enhanced by a different stabilizing mechanism, where the flow pattern perfectly fits within the geometry, resulting in more efficient fluid (and heat) transport (Chong et al., 2015). In our case we see yet again a stabilizing mechanism. Under the highly fluctuating angular motion a very stable (low fluctuations) $r-z$ double convection roll arises which reaches higher (average) velocities for higher amplitude modulation. This stable flow pattern effectively transports hot (cold) fluid from the bottom (top) plate, towards the sidewalls, up (down) to about half height and then back to the bottom (top) plate through the middle of the cylinder. This explains both effects of fast mixing at the plates (due to high horizontal velocities close to the plate) and the large gradient at half height (since that is where the two circulations meet). These effects, in turn, provide an explanation for the increased Nusselt number in these cases.

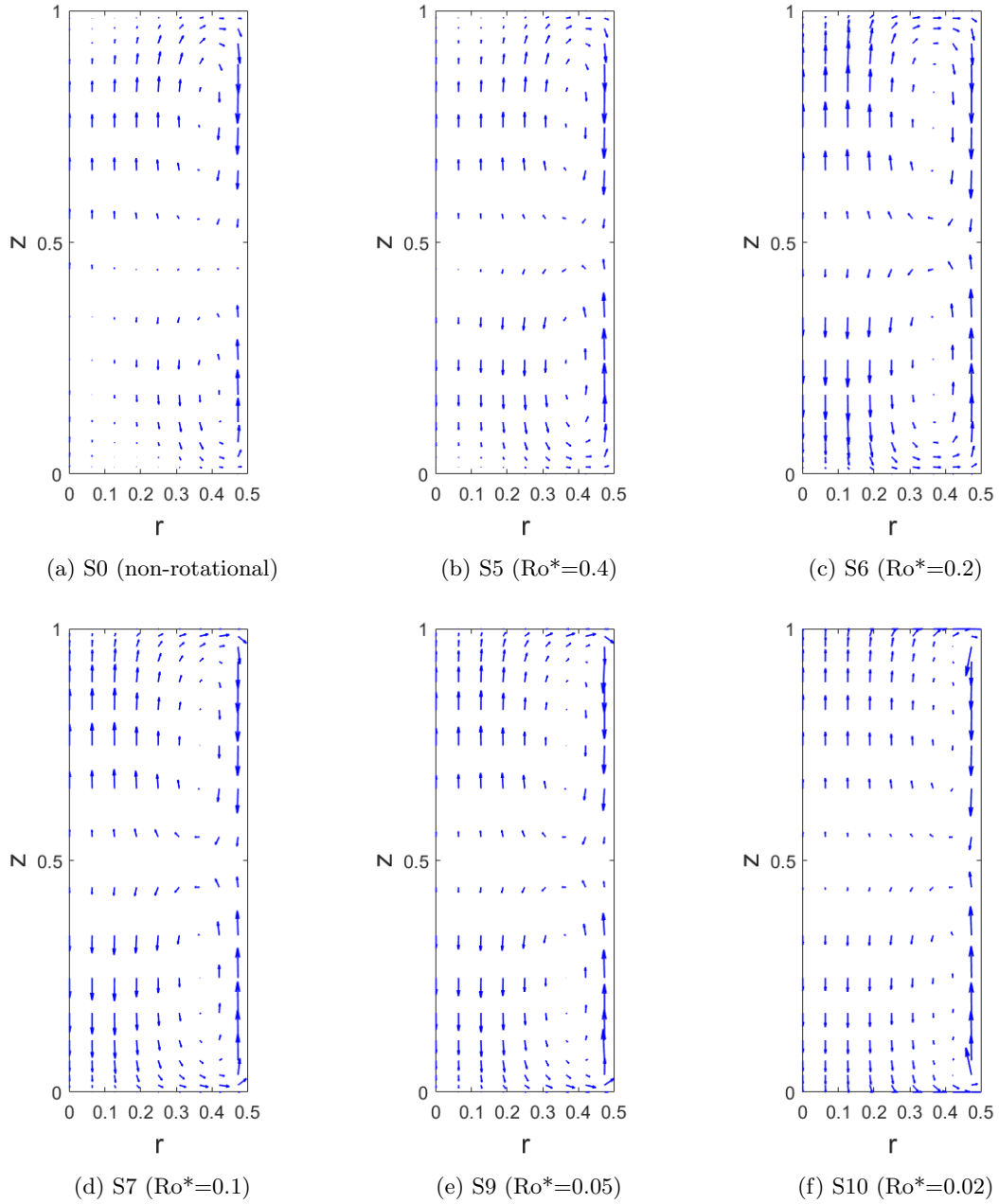


Figure 8: Vector plots for the mean (averaged over time and theta) radial and axial velocities for a (half) vertical slice through the cylinder. Arrow sizes are normalized independently, therefore equal arrows across subfigures do not represent equal velocities.

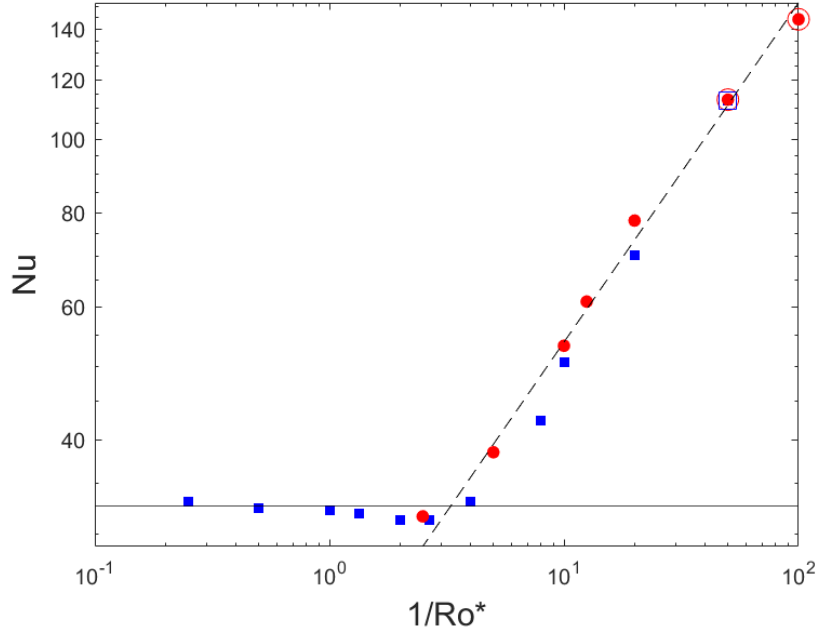


Figure 9: Achieved Nusselt values for the various simulations on a loglog scale. Blue squares: $Ro_\omega = 0.2$, including previous results by (Beunen and Kunnen, 2019); red circles: $Ro_\omega = 0.1$; horizontal line: Nusselt number for the non-rotating situation; dashed line: $y = c \cdot (Ro^*)^{-0.45}$. Open circles and square indicate the simulations with small scale structures which were not well-captured on the used simulation grid.

4 Increased Nusselt number for high amplitude, high frequency modulation

In Figure 9 the results for the Nusselt numbers are presented. They have been averaged over time and over the three different data sets that were obtained. For higher amplitudes (lower Rossby numbers) the Nusselt number increases extremely up to a 335% enhancement compared to the non-rotational case for the lowest amplitude of $Ro^*=0.01$. Instead of finding an optimal value of Ro^* , we instead see an asymptotic behaviour that sets on from about $Ro^* < 0.2$. Furthermore, whereas significant influence of Ro_ω was found by Beunen for lower amplitudes, this influence vanishes for this asymptotic region. In Figure 9 a potential scaling is plotted through our data points with formula $y = 19.1 \cdot (Ro^*)^{-0.45}$. These constants were based on the data that was obtained. In Figure 16 in the appendix a compensated graph can be found for this possible scaling of $(Ro^*)^{-0.45}$. Such a compensated graph magnifies the differences between the data and the proposed scaling law. In this case the values are quite close, and a scaling law of $(Ro^*)^{-0.45}$ could be possible. We have however not found a physical reasoning that would imply such a scaling.

In Figure 10 some time series for the Nusselt number are shown for simulations with different amplitudes. For all simulations it can be seen that the Nusselt number fluctuates over time. For the higher amplitudes these fluctuations are more extreme. In spite of these fluctuations the Nusselt number consistently remains at a significantly increased value, which confirms that the underlying flow structure shows stability in enhancing the heat transfer. Lastly, it must be mentioned that the large fluctuations at $Ro^*=0.02$ might also be due to the under-captured small scale structures for this simulation.

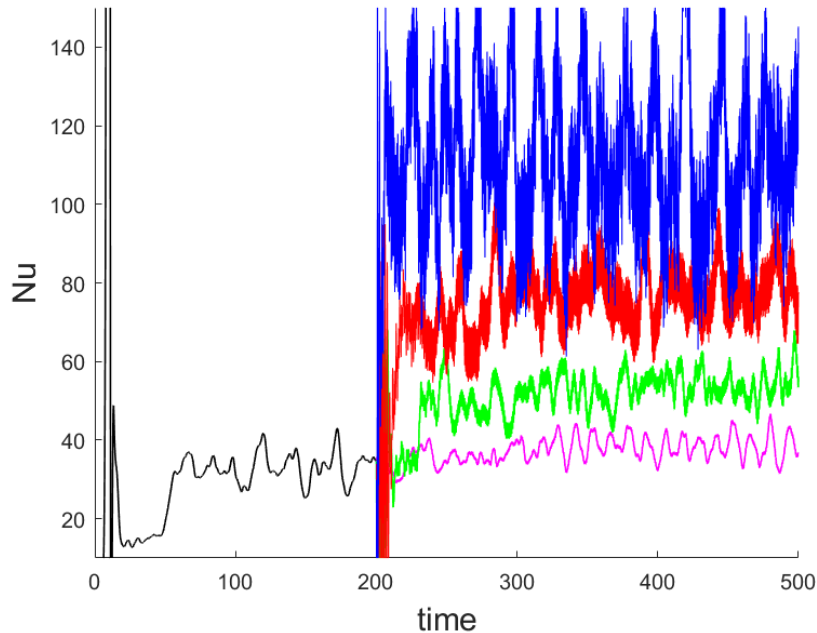


Figure 10: Time signals from the volume averaged derivation of the Nusselt number (equation 31). Black: non-rotational (S0); magenta: $Ro^*=0.2$ (S6); green: $Ro^*=0.1$ (S7); red: $Ro^*=0.05$ (S9); blue: $Ro^*=0.02$ (S10).

5 Concluding remarks

Direct numerical simulations were conducted for MRRB convection in a cylindrical domain. Based on the hypothesis of the bachelor project by Bob Beunen, this study provides a broader parameter sweep which confirms that indeed incredibly high Nusselt numbers can be achieved, a quadruplication compared to the non-rotational equivalent for these fluid parameters. The added Euler force for this type of RB convection causes an alternative stabilizing mechanism to emerge, different from the LSC and vertical plumes that are found in confined and rotational RB convection respectively. Despite the dominant angular fluctuations, a surprisingly stable double convection roll structure appears in the $r - z$ plane. The average velocity of these convection rolls seems to correlate with the amplitude of the modulation resulting in an asymptotic behaviour which seems to follow a scaling law. Attention needs to be given to optimizing the simulation process, as the main limiting factor of this research has proven to be the computational time. This could be done by looking into options for parallel simulation on multiple cores. A lower computational cost would pave the way for repeating such a parameter sweep at higher Rayleigh numbers, whilst taking better care of the resolution requirements. It will be worthwhile to see whether the flow structure in this asymptotic region holds for different fluid parameters. Lastly, more experimental results alongside the DNS would benefit this research. It remains to be seen whether the found asymptotic region is achievable in an experimental setting, although the study by Niemela et al shows promising results in this direction. Experimental verification of this effect could subsequently open up possibilities for industrial applications of modulated rotating Rayleigh-Bénard convection.

References

- Beunen, J. M. P. and Kunnen, R. P. J. (2019). Harmonically modulated rotating Rayleigh-Bénard convection.
- Cattaneo, F., Emonet, T., and Weiss, N. (2003). On the interaction between convection and magnetic fields. *Astrophysics Journal*, 588:1183–1198.
- Chong, K. L., Huang, S.-D., Kaczorowski, M., and Xia, K.-Q. (2015). Condensation of Coherent Structures in Turbulent Flows. *Physical Review Letters*, 115:264503.
- Geurts, B. J. and Kunnen, R. P. (2014). Intensified heat transfer in modulated rotating Rayleigh-Bénard convection. *International journal of heat and fluid flow*, 49:62–68.
- Glatzmaier, G., Coe, R., Hongre, L., and Roberts, P. (1999). A 3-dimensional self-consistent computer simulation of a geomagnetic field reversal. *Nature*, 401:885.
- Kooij, G. L., Botchev, M. A., Frederix, E. M. A., Geurts, B. J., Horn, S., Lohse, D., van der Poel, E. P., Shishkina, O., Stevens, R. J. A. M., and Verzicco, R. (2018). Comparison of computational codes for direct numerical simulations of turbulent Rayleigh-Bénard convection. *Computers & Fluids*, 166:1–8.
- Kunnen, R. (2008). *Turbulent rotating convection*. PhD Thesis Technische Universiteit Eindhoven.
- Niemela, J., Babuin, S., and Sreenivasan, K. (2010). Turbulent rotating convection at high Rayleigh and Taylor numbers. *Journal of fluid mechanics*, 649:509–522.
- Sidorenkov, N. (2009). *The Interaction Between Earth’s Rotation and Geophysical Processes*. Wiley-VCH.
- Stevens, R. J. A. M., Clercx, H. J. H., and Lohse, D. (2012). Breakdown of the large-scale circulation in $\gamma = 1/2$ rotating Rayleigh-Bénard flow. *Physical Review E*, 86:056311.
- Stevens, R. J. A. M., Clercx, H. J. H., and Lohse, D. (2013). Heat transport and flow structure in rotating Rayleigh-Bénard convection. *European Journal of Mechanics B/Fluids*, 40:41–49.
- Verzicco, R. and Orlandi, P. (1996). A finite-difference scheme for three-dimensional incompressible flows in cylindrical coordinates. *Journal of Computational Physics*, 123(2):402–414.
- Wu, J.-Z., Ma, H.-Y., and Zhou, M.-D. (2006). *Vorticity and Vortex Dynamics*. Springer-Verlag.

6 Appendix

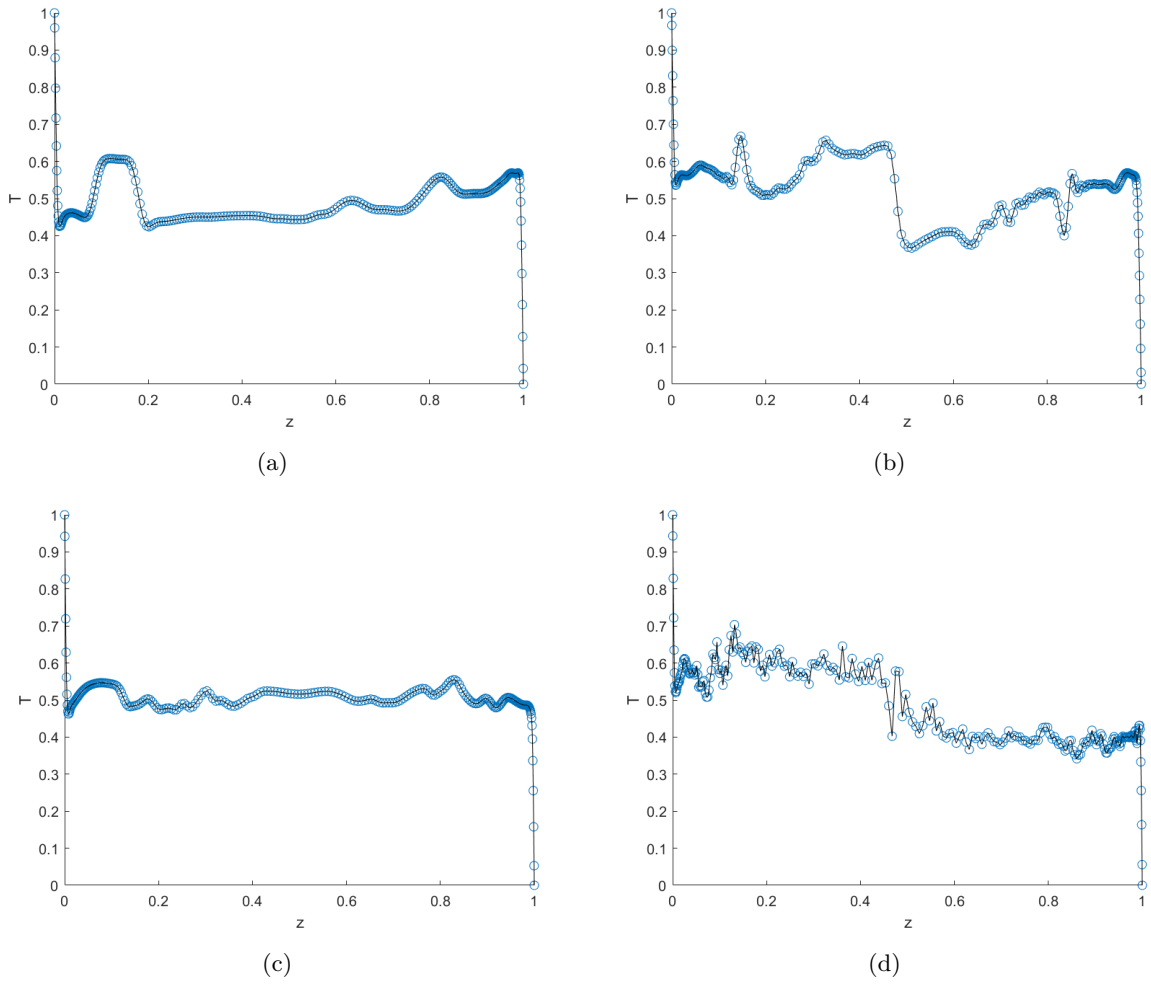


Figure 11: Temperature gradient along a vertical line; $Ro^* = 0.05, Ro_\omega = 0.1, time = 500$ for (a) $r = 0.08$ (in the bulk) and (b) $r = 0.47$ (close to the sidewall); $Ro^* = 0.02, Ro_\omega = 0.1, time = 500$ for (c) $r = 0.08$ (in the bulk) and (d) $r = 0.47$ (close to the sidewall).

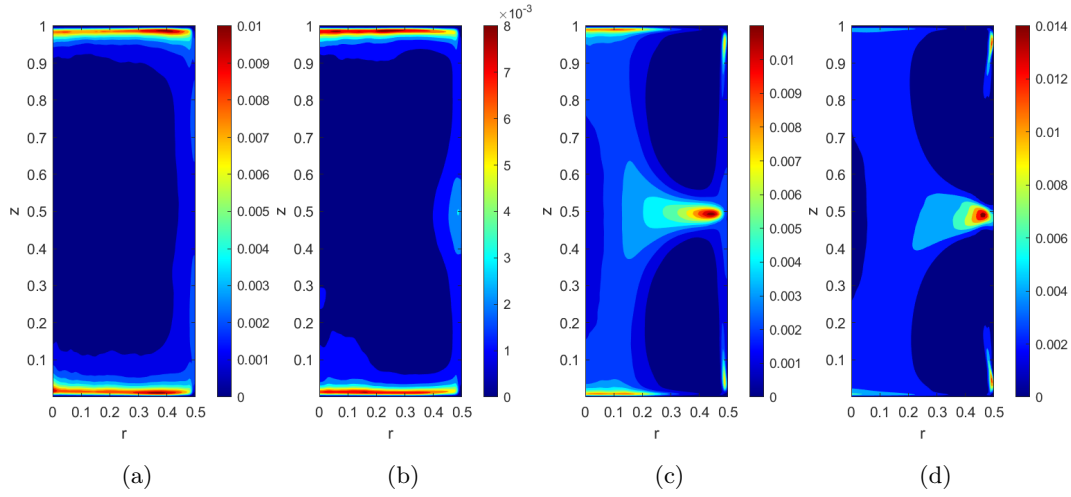


Figure 12: Temperature fluctuations (RMS) for simulations (a) S0, non-rotational; (b) S5, $Ro^*=0.4$; (c) S7, $Ro^*=0.1$; (d) S9, $Ro^*=0.05$.

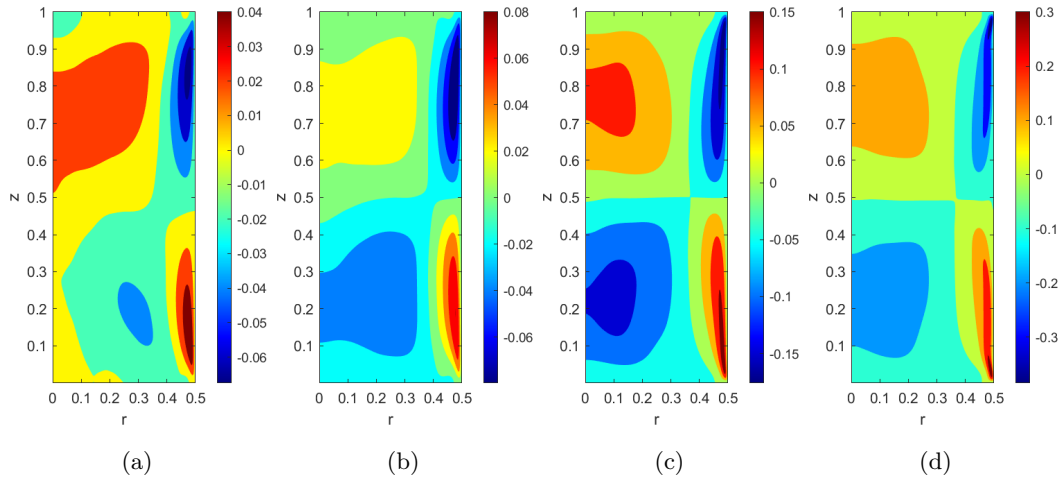


Figure 13: Mean vertical velocity for simulations (a) S0, non-rotational; (b) S5, $Ro^*=0.4$; (c) S7, $Ro^*=0.1$; (d) S9, $Ro^*=0.05$.

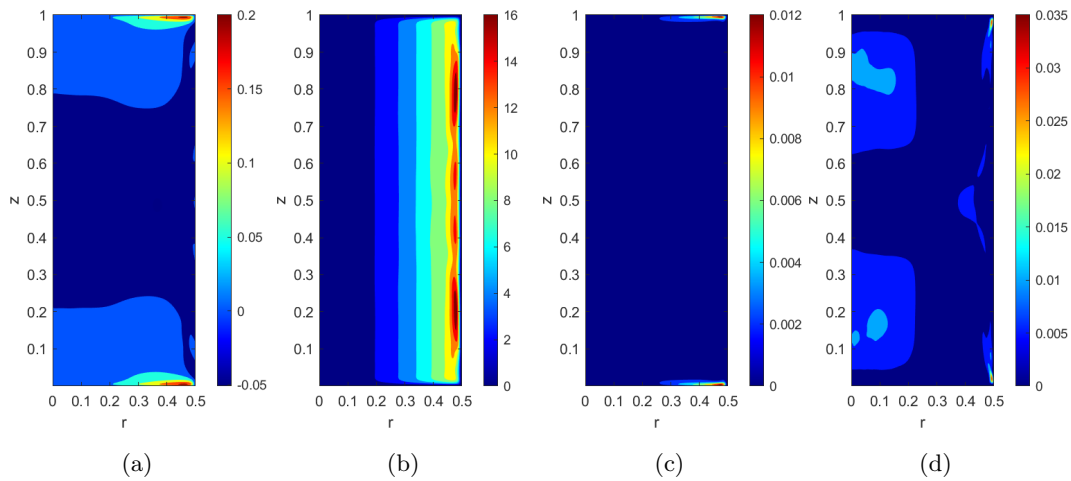


Figure 14: Additional statistical quantities for simulation S9 ($Ro^*=0.05$); (a) mean radial velocity, (b) angular fluctuations (RMS), (c) radial fluctuations (RMS) and (d) axial fluctuations (RMS).

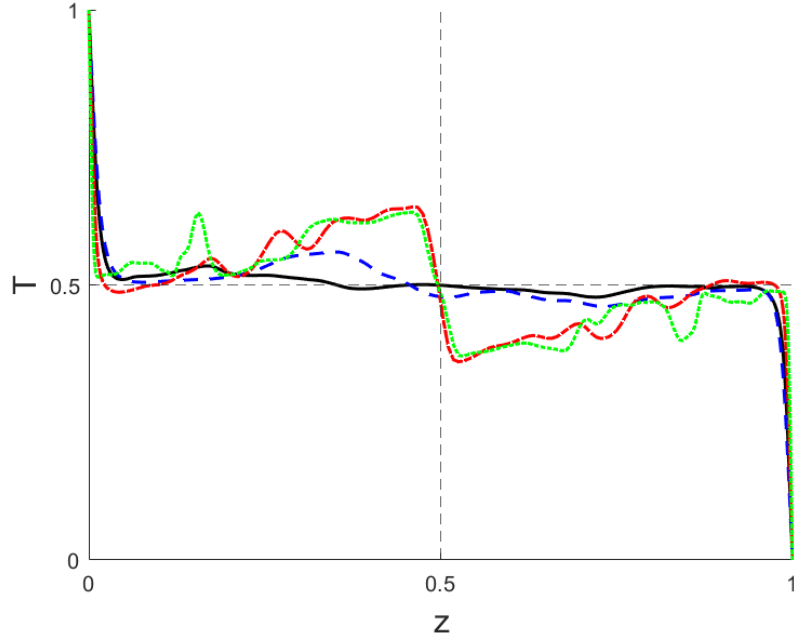


Figure 15: Angular-averaged temperature as function of height, close to the sidewall at $r \approx 0.47$. For simulations S0, non-rotational (black solid line), S5, $Ro^*=0.4$ (blue long dashed line), S7, $Ro^*=0.1$ (red short dashed line) and S9, $Ro^*=0.05$ (green dotted line). Vertical and horizontal dashed lines represent half height and average temperature respectively.

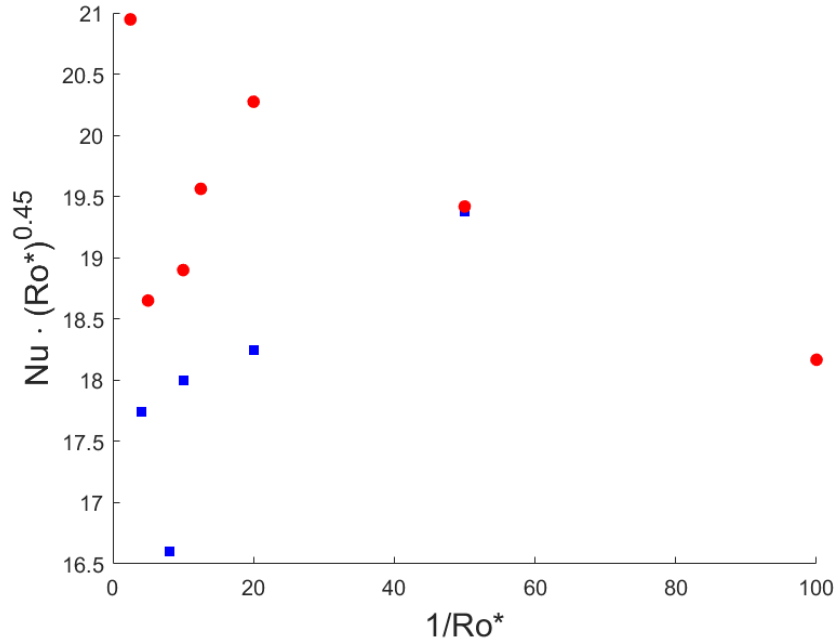


Figure 16: Compensated Nusselt values $Nu \cdot (Ro^*)^{0.45}$ for the various simulations. Blue squares: $Ro_\omega = 0.2$, including some previous results by (Beunen and Kunnen, 2019); red circles: $Ro_\omega = 0.1$